Ferroelectric control of the semiconductor-metal transition in two-dimensional MSi_2P_4/Sc_2CO_2 (M = Mo, W) van der Waals heterostructures and application to nonvolatile memory devices

Guogang Liu and San-Huang Ke*

MOE Key Laboratory of Microstructured Materials, School of Physics Science and Engineering, Tongji University, Shanghai 200092, People's Republic of China

(Received 12 November 2023; revised 12 December 2023; accepted 26 March 2024; published 17 April 2024)

The integration of two-dimensional (2D) ferroelectrics with other materials holds immense significance for exploring physics at the nanoscale. In this work, we systematically investigate the electronic and transport properties of 2D $MoSi_2P_4/Sc_2CO_2$ and WSi_2P_4/Sc_2CO_2 ferroelectric van der Waals heterostructures using density-functional theory and the nonequilibrium Green function method. The results reveal that the semiconductor-metal transition of $MoSi_2P_4$ and WSi_2P_4 monolayers can be flexibly realized by switching the ferroelectric polarization of the Sc_2CO_2 monolayer. Moreover, the metallicity of $MoSi_2P_4$ and WSi_2P_4 monolayers is further enhanced as the thickness of the ferroelectric layer increases, and the clamped sandwich structure also allows the nonvolatile electrical control of the metallicity of these two materials. Accordingly, proof-of-concept diodes based on $MoSi_2P_4/Sc_2CO_2$ and WSi_2P_4/Sc_2CO_2 heterostructures exhibit giant current ON:OFF ratios of up to 10^6 and 10^5, respectively. These findings not only provide viable strategies to realize and control metallicity in 2D semiconductors, but also offer promising candidates for the design of advanced memories.

DOI: 10.1103/PhysRevApplied.21.044033

I. INTRODUCTION

Constrained by the von Neumann bottleneck and the storage-wall problem, traditional silicon-based memories have gradually failed to fulfill the demands for massive data processing and storage [1–3]. Consequently, revolutionary memory technologies with ultrafast speed, ultrahigh capacity, and ultralow power consumption based on alternative principles, materials, and structures are highly favored [4,5]. Among the potential candidates, emerging two-dimensional (2D) materials and their heterostructures make efficient electrostatic modulation and nonvolatile storage possible due to their ideal atomically flat surfaces and immunity to short-channel effects [6–8].

Recently, Hong, Novoselov, and co-workers prepared an alternative family of 2D materials, MA_2Z_4 (M = early transition metal; A = Si or Ge; Z = N, P, or As), and synthesized $MoSi_2N_4$ and WSi_2N_4 monolayers in this family by the chemical vapor deposition method [9–11]. Owing to the compositional richness and structural diversity, theoretical calculations predict that the MA_2Z_4 materials will exhibit a wealth of physical and chemical characteristics, such as extraordinary ambient air stability, high carrier mobility, and tunable band gaps [12]. These intriguing features make the MA_2Z_4 family promising for applications in nanoelectronic devices, including field-effect transistors, nonvolatile memories, gas sensors, and magnetic tunneling junctions [13–17]. Up to now, numerous studies have focused on the modulation of the electronic structure of MA_2Z_4 materials through external strategies like strain engineering [12,18], external electric fields [18], carrier doping, and chemical decoration to facilitate their applications in the field of nanodevices [13,15,19,20]. For example, due to the built-in electric field induced by asymmetric charge transfer between two inner sublayers near the interface, the $MoSi_2N_4$ bilayer undergoes a semiconductor-to-metal transition at a critical vertical strain of around 22%, which opens up the possibility of fabricating electromechanical devices using these recently synthesized 2D materials [9,10,21]. Nevertheless, these state-of-the-art control methods are volatile and require continuous external control; otherwise, the induced state cannot be maintained. Therefore, the quest for a plausible method to achieve nonvolatile control of the 2D MA_2Z_4 family is still in progress.

With the continuous discovery of 2D materials, 2D ferroelectric monolayers provide a different platform for tuning the electrical properties of van der Waals (vdW) heterostructured materials due to the existence of electrically switchable spontaneous ferroelectric polarization [22–26]. In particular, theoretical studies have demonstrated that the ferromagnetic materials can be reversibly

*Corresponding author: shke@tongji.edu.cn

switched between semiconducting and half-metallic properties by nonvolatile control of the ferroelectric layer polarization states, which is highly advantageous for realizing nonvolatile storage [27–29]. However, 2D materials with an intrinsic magnetic nature are uncommon and usually require complex nanofabrication techniques [30–33]. Moreover, the two intrinsically ferromagnetic materials that have been successfully synthesized, namely, CrI_3 (45 K) and $Cr_2Ge_2Te_6$ (61 K), exhibit Curie temperatures, T_c, much lower than room temperature [34,35], which considerably limits their application in nanodevices. Therefore, the room-temperature-stable MA_2Z_4 family seems to be more fascinating and practical for nonvolatile-memory design. In light of this, the following pending questions immediately arise. Can MA_2Z_4 monolayers be combined with 2D ferroelectrics to form structurally stable vdW heterostructures? What are the electronic characteristics of such ferroelectric heterostructures? Can such ferroelectric heterostructures be used for device design, and what is the device performance?

Here, we implement the strategy of combining $MoSi_2P_4$ and WSi_2P_4 monolayers with a ferroelectric Sc_2CO_2 monolayer to design vdW heterostructures to address the above questions. Based on first-principles calculations, our results show that the semiconductor-metal transition of $MoSi_2P_4$ and WSi_2P_4 monolayers can be flexibly realized by switching the ferroelectric polarization of the Sc_2CO_2 monolayer. Also, combined with quantum transport simulations, we propose a prototype ferroelectric memory device based on $MoSi_2P_4/Sc_2CO_2$ and $MoSi_2P_4/Sc_2CO_2$ heterostructures, and the corresponding proof-of-concept diodes exhibit giant ON:OFF ratios of up to 10^6 and 10^5, respectively. Thus, our work reveals an effective method for exploring nonvolatile ferroelectric switches and memories.

II. COMPUTATIONAL DETAILS

The geometrical optimization and electronic structure calculations are performed using the Vienna *ab initio* simulation package [36], which is based on density-functional theory (DFT) with a plane-wave basis set and the projector-augmented wave method [37]. The exchange-correlation effects are described by the Perdew-Burke-Ernzerhof (PBE) with generalized gradient approximation [38]. A vacuum of about 20 Å is adopted to eliminate interactions between adjacent layers. The energy cutoff for the plane-wave basis functions is set to 500 eV. The structures are relaxed with an energy-convergence range of 10^{-6} eV, and the atomic force is less than 0.01 eV/Å. The first Brillouin-zone integrations are sampled with a $15 \times 15 \times 1$ k mesh [39]. The vdW interaction is described by the DFT-D3 method of Grimme *et al.* [40]. Considering that charge transfer in the systems can result in a net dipole moment, we consider dipole corrections in all calculations [41].

The quantum transport calculations are carried out by using the TranSIESTA code [42,43]. The cutoff energy is set to be 400 Ry. The basis type is the double-zeta basis plus polarization, and the k-point grids of $8 \times 1 \times 21$ are used for the self-consistent calculations of the central scattering region. The I-V curves of the diode systems are obtained by

$$I = \frac{2e^2}{h} \int dET(E,V)[f_S(E) - f_D(E)],$$

where T is the carrier transmission coefficient and $f_S(E)$ ($f_D(E)$) is the Fermi-Dirac distribution for the source (drain) electrode [44].

III. RESULTS AND DISCUSSION

A. Electronic structures of $MoSi_2P_4/Sc_2CO_2$ and WSi_2P_4/Sc_2CO_2 ferroelectric heterostructures

Before constructing the atomic models of the $M Si_2P_4/Sc_2CO_2$ (M = Mo, W) ferroelectric vdW heterostructures, we first investigate the geometric structures of $M Si_2P_4$ and Sc_2CO_2 monolayers, as shown in Figs. 1(a) and 1(b), respectively. The $M Si_2P_4$ and Sc_2CO_2 monolayers exhibit a hexagonal lattice with space groups of $P6m2$ (No. 187) and $P3m1$ (No. 156), respectively. Importantly, due to the asymmetric displacement of the inner C sublayer with respect to the Sc sublayer, the Sc_2CO_2 monolayer hosts intrinsic ferroelectricity with out-of-plane polarization [24,45]. The ferroelectric polarization state is denoted as $P\uparrow$ or $P\downarrow$ when the middle C sublayer is close to the top (C+) or the bottom (C−) O sublayer, respectively. The optimized in-plane lattice constants of the freestanding $M Si_2P_4$ and Sc_2CO_2 monolayers are 3.46 (for M = Mo; 3.47 for M = W) and 3.44 Å, respectively, which are consistent with previously reported results [9,11,24,45]. Note that the lattice mismatches in $MoSi_2P_4/Sc_2CO_2$ and WSi_2P_4/Sc_2CO_2 heterostructures are only 0.58% and 0.86%, allowing high experimental feasibility.

To obtain energetically favorable interfacial stacking configurations for $MoSi_2P_4/Sc_2CO_2$ and WSi_2P_4/Sc_2CO_2 heterostructures with both polarization states ($P\uparrow$ and $P\downarrow$), we considered six typical alignments between $M Si_2P_4$ and Sc_2CO_2 monolayers, as illustrated in Figs. 1(c) and 1(d). Here, when the P, Mo (W), and Si atoms in the $M Si_2P_4$ monolayer are aligned directly above the C atoms in the Sc_2CO_2 monolayer, the stacking configurations are denoted as CP-$P\uparrow/P\downarrow$, CM-$P\uparrow/P\downarrow$, and CSi-$P\uparrow/P\downarrow$, respectively. To assess the stability of these stacking systems, we calculate the interface binding energy, E_b, by using $E_b = E_{\text{total}} - E_M - E_{\text{Sc}}$, where E_{total}, E_M, and E_{Sc} are the total energies of the heterostructure, $M Si_2P_4$ monolayer, and Sc_2CO_2 monolayer, respectively. The related

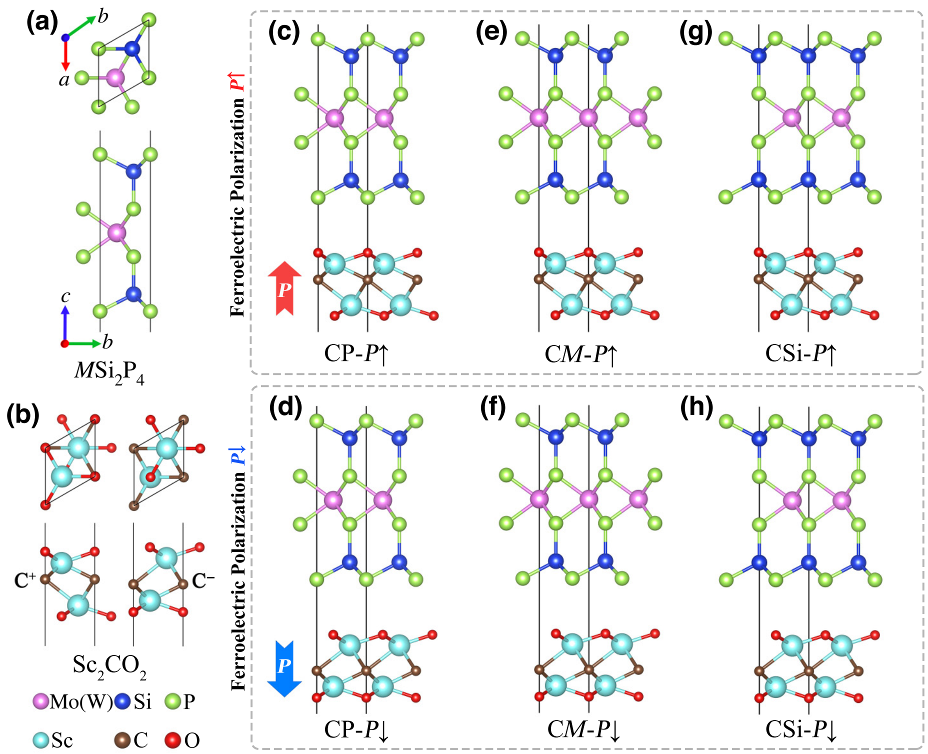

FIG. 1. Top and side views of (a) MSi_2P_4 (M = Mo, W) and (b) Sc_2CO_2 monolayers. Pink, blue, green, cyan, brown, and red balls represent Mo or W, Si, P, Sc, C, and O atoms, respectively. Side views of the $MoSi_2P_4/Sc_2CO_2$ and WSi_2P_4/Sc_2CO_2 heterostructures with different stacking configurations under polarized directions of (c) P↑ and (d) P↓.

interlayer spacings, binding energies, total energies, and band gaps of the $MoSi_2P_4/Sc_2CO_2$ and WSi_2P_4/Sc_2CO_2 heterostructures in different stacking configurations are listed in Table S1 within the Supplemental Material [46]. Clearly, the SiC-P↑/P↓ system exhibits the lowest binding energy, so we selected this stacking configuration as a representative to explore the electronic structures and transport properties of the $MoSi_2P_4/Sc_2CO_2$ ($MoSi_2P_4$-P↑/P↓) and WSi_2P_4/Sc_2CO_2 (WSi_2P_4-P↑/P↓) ferroelectric heterostructures. Also, to further confirm the stability of the constructed ferroelectric systems, we calculated the phonon dispersion by taking $MoSi_2P_4$-P↑/P↓ as an example. As depicted in Fig. S1 within the Supplemental Material [46], no imaginary phonon branch can be found in the whole Brillouin zone, indicating that these configurations are dynamically stable.

The band structures of isolated MSi_2P_4 and Sc_2CO_2 monolayers are shown in Figs. S2 and S3 within the Supplemental Material [46]. For $MoSi_2P_4$ and WSi_2P_4 monolayers, the conduction-band minimum (CBM) and valence-band maximum (VBM) are located at the K points, exhibiting direct band gaps of 0.72(0.99) and 0.52(0.80) eV at the PBE(HSE06) level, respectively. The ferroelectric Sc_2CO_2 monolayer also exhibits semiconductor behavior with an indirect band gap of 1.83(2.90) eV, and an out-of-plane electric dipole magnitude of 0.096 e Å/unit cell. These results are consistent with previous works [9,11,24]. To investigate the effect of ferroelectric polarization on the electronic structures of the $MoSi_2P_4$ and WSi_2P_4 monolayers, we calculate the projected band structures of the $MoSi_2P_4/Sc_2CO_2$ and WSi_2P_4/Sc_2CO_2 heterostructures for the P↑ and P↓ states. As presented in Figs. 2(a)–2(d), when the $MoSi_2P_4$ monolayer is coupled with Sc_2CO_2-P↑ or -P↓, the electronic properties of both submonolayers undergo significant modifications compared to the pristine crystals. Remarkably, the $MoSi_2P_4$ and WSi_2P_4 monolayers show a semiconductor-to-metal transition upon contact with Sc_2CO_2-P↑ [see Figs. 2(a) and 2(c)]. In contrast, when the polarization state of the Sc_2CO_2 monolayer is changed to P↓, the $MoSi_2P_4$ and WSi_2P_4 monolayers remain semiconductors with band gaps of 0.72 and 0.51 eV [see Figs. 2(b) and 2(d)], respectively.

Since the electronic structures of the $MoSi_2P_4$-P↑/P↓ and WSi_2P_4-P↑/P↓ ferroelectric heterostructures are similar, we discuss the former in more detail. In the case of P↑, as shown in Fig. 2(a), the CBM of the $MoSi_2P_4$ monolayer decreases by 0.71 eV and crosses the Fermi level, thus realizing the transition of the heterostructure to metallicity. Moreover, the $MoSi_2P_4$-P↑ system forms a type-III broken-gap band alignment, which may prove advantageous for applications in tunneling field-effect

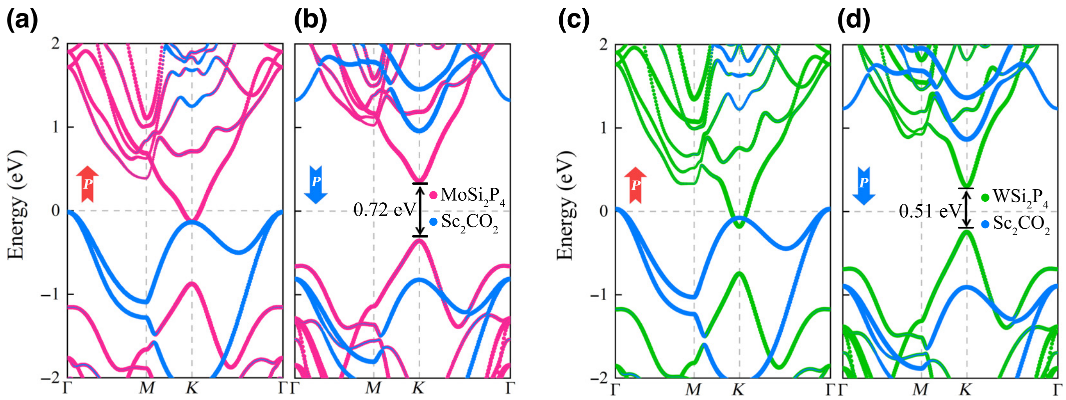

FIG. 2. Projected band structures of (a),(b) $MoSi_2P_4/Sc_2CO_2$ and (c),(d) WSi_2P_4/Sc_2CO_2 heterostructures under $P\uparrow$ and $P\downarrow$ states. Contributions of the $MoSi_2P_4$, WSi_2P_4, and Sc_2CO_2 monolayers to the band structures of the heterostructures are presented by magenta, green, and blue dotted lines, respectively.

transistors. In contrast, in the case of $P\downarrow$, as shown in Fig. 2(b), the CBM of the $MoSi_2P_4$ monolayer only changes by 0.18 eV, where the common band gap is maintained and the heterostructure exhibits semiconducting characteristics of type-I band alignment. Moreover, we examine the band structures by using the HSE06 functional, and found that the overall band structure of the heterostructure is well preserved (see Fig. S4 within the Supplemental Material [46]), indicating that the semiconductor-to-metal transition is robust and the prediction of physical properties by the PBE functional is reasonable. Furthermore, when the spin-orbit-coupling effect is included, the band structure of the ferroelectric heterostructure shows no significant variations (see Fig. S5 within the Supplemental Material [46]).

Indeed, an external electric field may reversibly switch the $P\uparrow$ and $P\downarrow$ states of the ferroelectric Sc_2CO_2 sublayer, and the energy barrier for its switching from the polar to nonpolar configuration is higher than that of the well-known perovskite ferroelectric $LiNbO_3$ [24,45]. Obviously, the Sc_2CO_2 monolayer retains its semiconducting nature in both cases, which allows the external electric field to switch its polarization state effectively [47]. Based on the bistable behavior of the $P\uparrow$ and $P\downarrow$ states, it can be inferred that the electrical switching between the two opposite polarization states is nonvolatile. In the $MoSi_2P_4/Sc_2CO_2$ and WSi_2P_4/Sc_2CO_2 heterostructures, the electronic properties of the $MoSi_2P_4$ and WSi_2P_4 monolayers are highly dependent on the polarization state of the ferroelectric Sc_2CO_2 monolayer, and thus, the switchable electrical control of the $MoSi_2P_4$ and WSi_2P_4 monolayers from semiconductors to metals via the Sc_2CO_2 monolayer is also nonvolatile. This kind of nonvolatile electrical control of 2D semiconductors realized by a ferroelectric switch may also be realized in other systems [45,48–50].

B. Mechanism of the semiconductor-metal transition modulated by ferroelectric polarization

In the following, we discuss the underlying physics of ferroelectric bistability and the interfacial coupling leading to the electrically controlled metallicity of the $M Si_2P_4$ monolayer. The strong coupling is attributed to the broken spatial inversion symmetry of the Sc_2CO_2 monolayer, and this will result in a different band alignment of the ferroelectric heterostructure system. As displayed in Fig. 3(b), the in-plane average electrostatic potential of the ferroelectric Sc_2CO_2 monolayer exhibits a significant difference in the out-of-plane direction compared to the symmetric $M Si_2P_4$ monolayer, which leads to different work functions on both sides. The calculated work functions of the $M Si_2P_4$ monolayer ($W_{\mathrm{Mo(W)}}$), "C+" side ($W_{\mathrm{C+}}$), and "C−" side ($W_{\mathrm{C-}}$) of the Sc_2CO_2 monolayer are 5.01 (for M = Mo; 4.79 for M = W), 3.45, and 5.26 eV, respectively, and in accordance with the relationship of $W_{\mathrm{C+}} < W_{\mathrm{W}} < W_{\mathrm{Mo}} < W_{\mathrm{C-}}$. It is well known that, when two different semiconductors are stacked together, electrons will flow from the sublayer with the lower work function to the other, causing the energy level on the side with the larger (smaller) work function to shift down (up) until the heterostructure system establishes a common Fermi level [51]. Therefore, different band alignments occur when the $M Si_2P_4$ monolayer is coupled with Sc_2CO_2-$P\uparrow$ or -$P\downarrow$, leading to different interfacial charge transfers [see Figs. 3(a) and S6(a) within the Supplemental Material [46]]. In the $M Si_2P_4$-$P\uparrow$ case, the work functions of the coupled interfaces are $W_{\mathrm{Mo(W)}}$ and $W_{\mathrm{C+}}$, respectively, which leads to the interface work function difference ($\triangle W$) up to 1.56(1.34) eV. Thus, the energy bands of the $M Si_2P_4$ monolayer will move down with respect to the Sc_2CO_2 monolayer. Since the band gap of the $M Si_2P_4$ monolayer [0.72(0.52) eV] is far smaller than $\triangle W$, the CBM of the $M Si_2P_4$ monolayer can move lower than the VBM of the Sc_2CO_2 monolayer [see Figs. 2(a) and 2(c)]. As a result, considerable electrons flow from the Sc_2CO_2 monolayer to the $M Si_2P_4$ monolayer, and the $M Si_2P_4$ monolayer turns into a conductor [see Figs. 3(a) and S6(a) within the Supplemental Material [46]]. On the contrary, in the $M Si_2P_4$-$P\downarrow$ case, the work functions of the contacted interfaces are $W_{\mathrm{Mo(W)}}$ and $W_{\mathrm{C}-}$, respectively, which results in a $\triangle W$ of only 0.25(0.47) eV. Although the energy bands of the Sc_2CO_2 monolayer will shift down relative to the $M Si_2P_4$ monolayer [see Figs. 2(b) and 2(d)], the CBM of the Sc_2CO_2 monolayer is impossibly lower than the VBM of the $M Si_2P_4$ monolayer, since the band gap of the Sc_2CO_2 monolayer (1.83 eV) is much greater than $\triangle W$ at this point. Consequently, the electrons are quite difficult to transfer from the Sc_2CO_2 monolayer to the $M Si_2P_4$ monolayer, and both materials remain semiconductors [see Figs. 3(a) and S6(a) within the Supplemental Material [46]].

To visualize the interfacial interaction and charge redistribution between the interfaces, the plane-averaged differential charge density ($\triangle\rho$) and the corresponding three-dimensional (3D) differential charge density are shown in Figs. 3(c) and S6(b) within the Supplemental Material [46]. The positive and negative values (red and green areas) represent electron accumulation and depletion, respectively. Clearly, the $M Si_2P_4$-$P\uparrow$ system exhibits significantly stronger charge redistribution at the interface than the $M Si_2P_4$-$P\downarrow$ system. For the $M Si_2P_4$-$P\uparrow$ system, the $M Si_2P_4$ monolayer acts as an acceptor and gains electrons, whereas the Sc_2CO_2 monolayer serves as a donor and mainly loses electrons, resulting in strong charge transfer at the interface. Conversely, when the polarization state of the Sc_2CO_2 monolayer switches from $P\uparrow$ to $P\downarrow$, charge transfer between $M Si_2P_4$ and $P\downarrow$ is almost negligible. In general, both charge accumulation and charge depletion constitute the interfacial charge redistribution, which leads to the formation of an interfacial electric dipole. The existence of such an interfacial dipole directly alters the interfacial band alignment [52], yielding the band-structure variation displayed in Figs. 2(a)–2(d).

C. Electronic structures of the ferroelectric heterostructure with a ferroelectric bilayer

To explore more possibilities of nonvolatile electrical control of the metallicity in the $M Si_2P_4$ monolayer, we further stack the $M Si_2P_4$ monolayer on the Sc_2CO_2 bilayer to form the trilayer ferroelectric vdW heterostructure, as shown in Fig. 4(a). Due to the robust covalent interactions between the C and O sublattices, the Sc_2CO_2 bilayer exhibits a larger potential difference with enhanced ferroelectric polarization [see Fig. S3(b) within the Supplemental Material [46]]. This behavior implies even stronger charge transfer when the $M Si_2P_4$ monolayer is in contact with the Sc_2CO_2 bilayer. Based on the polarization directions of both ferroelectric layers as $P\uparrow$ or $P\downarrow$, the corresponding configurations are denoted as $M Si_2P_4$-$P\uparrow\uparrow$ and $M Si_2P_4$-$P\downarrow\downarrow$, respectively. In the $M Si_2P_4$-$P\uparrow\uparrow$ case, as shown in Figs. 4(c) and S7(a) within the Supplemental Material [46], owing to the enhanced polarization field from the ferroelectric Sc_2CO_2 bilayer, the conduction-band energy of the $M Si_2P_4$ monolayer decreases by 0.86(0.76) eV, which is significantly larger than that in the $M Si_2P_4$-$P\uparrow$ system. Similar to the ferroelectric monolayer case, the conduction band of the $M Si_2P_4$ monolayer passes through the Fermi level and forms a more metallic band structure. On the contrary, in the case of $M Si_2P_4$-$P\downarrow\downarrow$, as shown in Figs. 4(d) and S7(b) within the Supplemental Material [46], the $M Si_2P_4$ monolayer maintains its semiconducting nature and the band gap increases to 0.75(0.56) eV. Therefore, the $M Si_2P_4$ monolayer can be flexibly converted from a semiconductor to a metal by switching the ferroelectric polarization of the

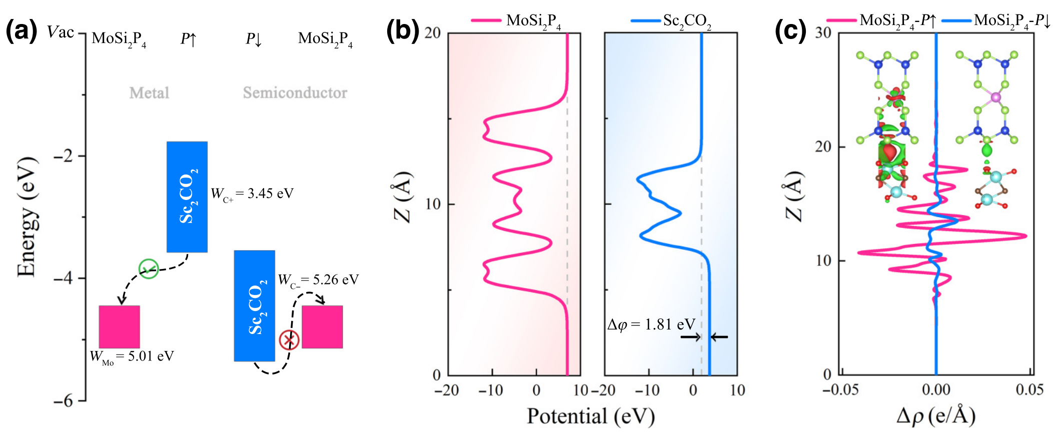

FIG. 3. (a) Band alignment of the $MoSi_2P_4/Sc_2CO_2$ heterostructure. (b) Planar average potential of the $MoSi_2P_4$ and Sc_2CO_2 monolayers. (c) Plane-averaged differential charge density ($\triangle\rho$) and corresponding 3D differential charge density of $0.0003e/\mathrm{bohr}^3$ isosurface. Red and green areas represent electron accumulation and depletion, respectively. Plane-averaged charge density along the z direction, $\rho(z)$, is defined as $\rho(z) = \int \Delta\rho(x, y, z)\, dx\, dy$.

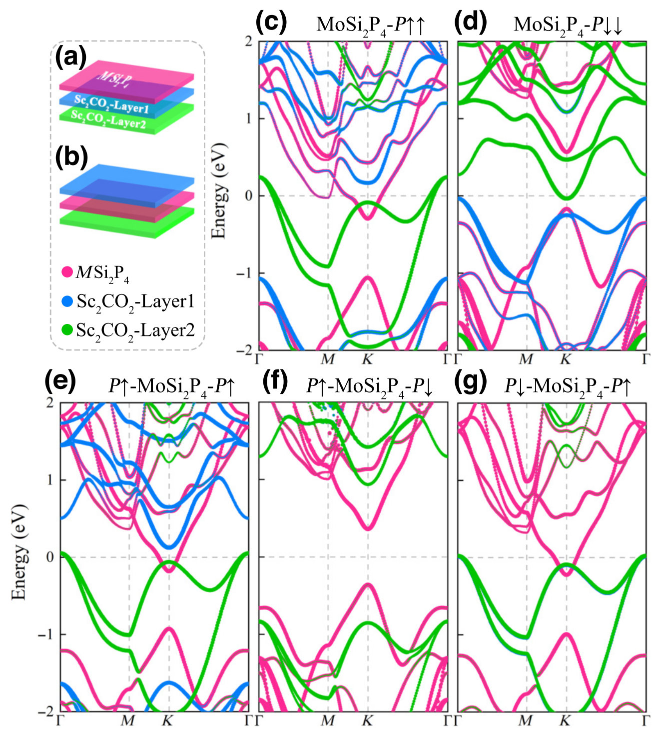

FIG. 4. Stacking schematic of (a) $M\mathrm{Si_2P_4/Sc_2CO_2}$ bilayer and (b) $\mathrm{Sc_2CO_2}/M\mathrm{Si_2P_4/Sc_2CO_2}$ vdW heterostructures. Projected band structures of (c),(d) $\mathrm{MoSi_2P_4/Sc_2CO_2}$ bilayer and (e)–(g) $\mathrm{Sc_2CO_2/MoSi_2P_4/Sc_2CO_2}$ clamped sandwich heterostructure. Contributions of the $\mathrm{MoSi_2P_4}$ monolayer and $\mathrm{Sc_2CO_2}$ bilayer to the band structures of the heterostructures are presented by magenta and green (blue) dotted lines, respectively.

$\mathrm{Sc_2CO_2}$ bilayer, and the metallicity is further enhanced due to greater electron transfer.

In addition, we also consider another three clamped sandwich heterostructures, where the $M\mathrm{Si_2P_4}$ monolayer is sandwiched between two ferroelectric $\mathrm{Sc_2CO_2}$ monolayers [see Fig. 4(b)], named $P\uparrow$-$M\mathrm{Si_2P_4}$-$P\uparrow$, $P\uparrow$-$M\mathrm{Si_2P_4}$-$P\downarrow$, and $P\downarrow$-$M\mathrm{Si_2P_4}$-$P\uparrow$. Note that the $M\mathrm{Si_2P_4}$ monolayer is metallic in both the $P\uparrow$-$M\mathrm{Si_2P_4}$-$P\uparrow$ and $P\downarrow$-$M\mathrm{Si_2P_4}$-$P\uparrow$ systems, whereas it is semiconducting in the $P\uparrow$-$M\mathrm{Si_2P_4}$-$P\downarrow$ system (see Figs. 4 and S7 within the Supplemental Material [46]). Therefore, the $M\mathrm{Si_2P_4}$ monolayer is only metallic when its upper (lower) surface is coupled with $\mathrm{Sc_2CO_2}$-$P\downarrow$ ($\mathrm{Sc_2CO_2}$-$P\uparrow$); otherwise, it remains semiconducting, which is consistent with the case of the ferroelectric monolayer. These results suggest that the electrically controlled metallicity of the $M\mathrm{Si_2P_4}$ monolayer can also be realized in the $\mathrm{Sc_2CO_2}$-$M\mathrm{Si_2P_4}$-$\mathrm{Sc_2CO_2}$ clamped sandwich structures, which provides more flexibility for designing alternative ferroelectric memories.

D. Prototype of a ferroelectric memory device and quantum transport simulations

Based on our theoretical results, we propose that the $\mathrm{MoSi_2P_4/Sc_2CO_2}$ and $\mathrm{WSi_2P_4/Sc_2CO_2}$ ferroelectric vdW heterostructures are ideal structures for designing nonvolatile memory devices. The proposed prototype ferroelectric memory device is shown in Fig. 5(a), where the $M\mathrm{Si_2P_4}$ layer acts as a selectively conducting channel and the $\mathrm{Sc_2CO_2}$ layer serves as a substrate responsible for providing different polarization states. Specifically, when the $\mathrm{Sc_2CO_2}$ layer is in the $P\uparrow$ state, electrons are allowed to travel in the channel due to the metallic nature of the $M\mathrm{Si_2P_4}$ layer, which represents the “ON” or “1” state of the device. On the contrary, when the $\mathrm{Sc_2CO_2}$ layer is switched to the $P\downarrow$ state, the $M\mathrm{Si_2P_4}$ layer becomes semiconducting and electron transmission in the channel is blocked, which corresponds to the “OFF” or “0” state of the device. Therefore, data writing in this memory device is realized by switching the ferroelectric polarized states, while data reading is achieved by detecting the electrical signals.

To validate the above concept, we constructed $\mathrm{MoSi_2P_4/Sc_2CO_2}$ and $\mathrm{WSi_2P_4/Sc_2CO_2}$ ferroelectric-heterostructure-based diodes. Each diode is composed of periodic source and drain electrodes and the central scattering region of the $\mathrm{MoSi_2P_4/Sc_2CO_2}$ ($\mathrm{WSi_2P_4/Sc_2CO_2}$) heterostructure. Specifically, the electrodes and the extended region of the device consist of three orthorhombic cells of the $\mathrm{MoSi_2P_4/Sc_2CO_2}$ ($\mathrm{WSi_2P_4/Sc_2CO_2}$) heterostructure with a lattice constant of 0.595(0.597) nm. Meanwhile, the central scattering region along the transport direction contains six orthorhombic cells and has a length of 3.570(3.582) nm. As shown in Fig. 5(b) and S9 within the Supplemental Material [46], the $\mathrm{MoSi_2P_4}$-$P\uparrow$ and $\mathrm{MoSi_2P_4}$-$P\downarrow$ systems exhibit significantly different behaviors under limited biases from 0 to 0.6 V. Explicitly, the I-V curve of the $\mathrm{MoSi_2P_4}$-$P\uparrow$-based diode displays a linear behavior similar to that of metals (ON or 1). However, as with semiconductors or insulators, the current through the $\mathrm{MoSi_2P_4}$-$P\downarrow$-based diode is almost zero (OFF or 0). The calculated I-V curve of the $\mathrm{WSi_2P_4}$-$P\uparrow$ (-$P\downarrow$) system is shown in Fig. S8(a) within the Supplemental Material [46], and it can be seen that the variation of the two opposite polarization states is consistent with that of the $\mathrm{MoSi_2P_4}$-$P\uparrow$ ($-P\downarrow$) system. Meanwhile, the transmission spectra of the $\mathrm{MoSi_2P_4/Sc_2CO_2}$-based diode as a function of the electron energy and bias voltage is displayed in Fig. 5(c). Note that the electron-transmission probability of the $P\uparrow$ state is much higher than that of the $P\downarrow$ state for the same electron energy and bias voltage. Also, the pink region within the bias window of the $P\downarrow$ system is barely visible, which confirms the extremely low current of the diode in the $P\downarrow$ state.

Considering that the constructed diode exhibits significant ON:OFF switching between $P\uparrow$ and $P\downarrow$ states, we further calculated the current ON:OFF ratio based on the I-V curves of Figs. 5(b) and S8(a) within the Supplemental Material [46]. It is found that the ferroelectric diodes based on the $\mathrm{MoSi_2P_4/Sc_2CO_2}$ and $\mathrm{WSi_2P_4/Sc_2CO_2}$ heterostructures have giant ON:OFF ratios at the limited bias voltage,

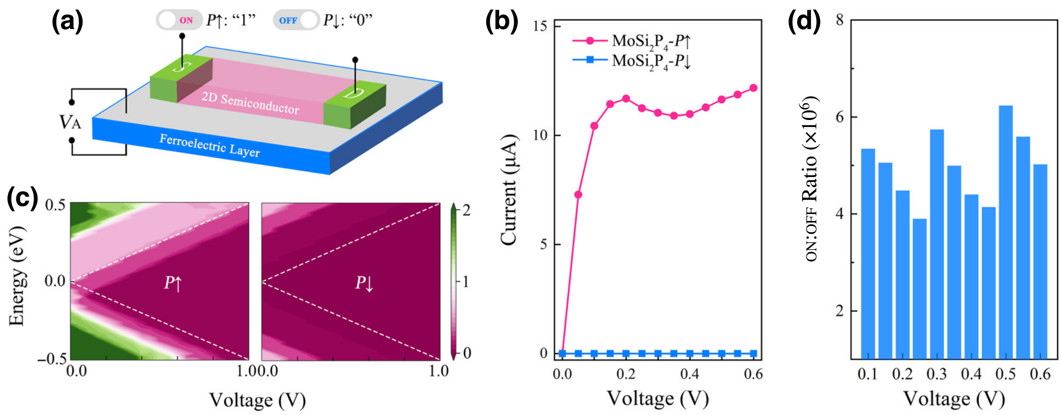

FIG. 5. (a) Prototypes of the ferroelectric memory device based on $MoSi_2P_4/Sc_2CO_2$ and WSi_2P_4/Sc_2CO_2 vdW heterostructures. (b) *I-V* curves and (c) transmission spectra as a function of bias voltage and electron energy of the $MoSi_2P_4$-*P*↑ and $MoSi_2P_4$-*P*↓ ferroelectric diodes. (d) ON:OFF ratio of $MoSi_2P_4/Sc_2CO_2$-based diode at different bias voltages.

and the ON:OFF ratios are consistently larger than 1×10^6 and 1×10^5 [see Figs. 5(c) and S8(b) within the Supplemental Material [46]], respectively; these are several orders of magnitude larger than those previously reported for 2D multiferroic systems [48,49]. Therefore, we theoretically demonstrate that the proposed $MoSi_2P_4/Sc_2CO_2$ and WSi_2P_4/Sc_2CO_2 ferroelectric heterostructures can realize the two ideal 0 and 1 states in data storage.

IV. CONCLUSION

We have investigated vdW heterostructures formed by stacking the MSi_2P_4 monolayer on a ferroelectric Sc_2CO_2 monolayer or bilayer using first-principles calculations. The results show that the $MoSi_2P_4$ and WSi_2P_4 monolayers undergo a semiconductor-metal transition upon contact with Sc_2CO_2-*P*↑, while both monolayers maintain their intrinsic semiconducting nature when the polarization state of the Sc_2CO_2 monolayer switches from *P*↑ to *P*↓. Moreover, the metallicity of the $MoSi_2P_4$ and WSi_2P_4 monolayers is further enhanced as the thickness of the ferroelectric layer increases, and the clamped sandwich structures can also flexibly modulate the semiconductor-metal transitions of these two materials. The reversible switching endows MSi_2P_4/Sc_2CO_2 and MSi_2P_4/Sc_2CO_2 heterostructures with numerous promising applications in nanodevices, such as atom-thick ferroelectric memories. Accordingly, transport calculations reveal that the proof-of-concept diodes based on the $MoSi_2P_4/Sc_2CO_2$ and WSi_2P_4/Sc_2CO_2 heterostructures exhibit giant current ON:OFF ratios of up to 10^6 and 10^5, respectively. These findings demonstrate an alternative approach to control semiconductor-metal transitions for 2D materials by ferroelectric polarizations, which has the advantage of nonvolatility and is useful for future memory device applications.

ACKNOWLEDGMENTS

This work was supported by the Natural Science Foundation of Shanghai under Grant No. 19ZR1459100 and the National Natural Science Foundation of China under Grant No. 11374226.

[1] G. E. Moore, Cramming more components onto integrated circuits, Proc. IEEE **86**, 82 (1998).

[2] A. D. Franklin, Nanomaterials in transistors: From high-performance to thin-film applications, Science **349**, aab2750 (2015).

[3] S. Salahuddin, K. Ni, and S. Datta, The era of hyper-scaling in electronics, Nat. Electron. **1**, 442 (2018).

[4] K. Novoselov, A. Mishchenko, A. Carvalho, and A. Castro Neto, 2D materials and van der Waals heterostructures, Science **353**, aac9439 (2016).

[5] X. Liu and M. C. Hersam, 2D materials for quantum information science, Nat. Rev. Mater. **4**, 669 (2019).

[6] S. H. Choi, S. J. Yun, Y. S. Won, C. S. Oh, S. M. Kim, K. K. Kim, and Y. H. Lee, Large-scale synthesis of graphene and other 2D materials towards industrialization, Nat. Commun. **13**, 1484 (2022).

[7] Y. Liu, X. Duan, H. Shin, S. Park, Y. Huang, and X. Duan, Promises and prospects of two-dimensional transistors, Nature **591**, 43 (2021).

[8] S. Wang, X. Liu, and P. Zhou, The road for 2D semiconductors in the silicon age, Adv. Mater. **34**, 2106886 (2022).

[9] Y. Hong, Z. Liu, L. Wang, T. Zhou, W. Ma, C. Xu, S. Feng, L. Chen, M. Chen, and D. Sun, Chemical vapor deposition of layered two-dimensional $MoSi_2N_4$ materials, Science **369**, 670 (2020).

[10] K. S. Novoselov, Discovery of 2D van der Waals layered $MoSi_2N_4$ family, Nat. Sci. Rev. **7**, 1842 (2020).

[11] L. Wang, Y. Shi, M. Liu, A. Zhang, Y. Hong, R. Li, Q. Gao, M. Chen, W. Ren, and H. Cheng, Intercalated architecture of MA_2Z_4 family layered van der Waals materials

with emerging topological, magnetic and superconducting properties, Nat. Commun. **12**, 2361 (2021).

[12] B. Mortazavi, B. Javvaji, F. Shojaei, T. Rabczuk, A. V. Shapeev, and X. Zhuang, Exceptional piezoelectricity, high thermal conductivity and stiffness and promising photocatalysis in two-dimensional $MoSi_2N_4$ family confirmed by first-principles, Nano Energy **82**, 105716 (2021).

[13] J. Huang, P. Li, X. Ren, and Z. Guo, Promising properties of a sub-5-nm monolayer $MoSi_2N_4$ transistor, Phys. Rev. A **16**, 044022 (2021).

[14] T. Zhong, Y. Ren, Z. Zhang, J. Gao, and M. Wu, Sliding ferroelectricity in two-dimensional MoA_2N_4 (A = Si or Ge) bilayers: High polarizations and Moiré potentials, J. Mater. Chem. A **35**, 19659 (2021).

[15] L. Yan, B. Wang, X. Huang, Q. Li, K. Xue, J. Zhang, W. Ren, and L. Zhou, Surface passivation induced a significant enhancement of superconductivity in layered two-dimensional MSi_2N_4 (M = Ta and Nb) materials, Nanoscale **13**, 18947 (2021).

[16] R. Islam, B. Ghosh, C. Autieri, S. Chowdhury, A. Bansil, A. Agarwal, and B. Singh, Tunable spin polarization and electronic structure of bottom-up synthesized $MoSi_2N_4$ materials, Phys. Rev. B **104**, L201112 (2021).

[17] Y. Gao, J. Liao, H. Wang, Y. Wu, Y. Li, K. Wang, C. Ma, S. Gong, T. Wang, X. Dong, Z. Jiao, and Y. An, Electronic transport properties and nanodevice designs for monolayer $MoSi_2P_4$, Phys. Rev. A **18**, 034033 (2022).

[18] Q. Wu, L. Cao, Y. S. Ang, and L. K. Ang, Semiconductor-to-metal transition in bilayer $MoSi_2N_4$ and WSi_2N_4 with strain and electric field, Appl. Phys. Lett. **118**, 113102 (2021).

[19] L. Cao, G. Zhou, Q. Wang, L. K. Ang, and Y. S. Ang, Two-dimensional van der Waals electrical contact to monolayer $MoSi_2N_4$, Appl. Phys. Lett. **118**, 013106 (2021).

[20] Q. Wang, L. Cao, S. Liang, W Wu, G Wang, L. K. Ang, and Y. S. Ang, Efficient Ohmic contacts and built-in atomic sublayer protection in $MoSi_2N_4$ and WSi_2N_4 monolayers, npj 2D Mater. Appl. **5**, 71 (2021).

[21] H. Zhong, J. Zhu, W. Xiong, P. Lv, J. Yu, and S. Yuan, Strain-induced semiconductor to metal transition in MA_2Z_4 bilayers (M = Ti, Cr, Mo; A = Si; Z = N, P), Phys. Rev. B **103**, 085124 (2021).

[22] W. Ding, J. Zhu, Z. Wang, Y. Gao, D. Xiao, Y. Gu, Z. Zhang, and W. Zhu, Prediction of intrinsic two-dimensional ferroelectrics in In_2Se_3 and other III_2–VI_3 van der Waals materials, Nat. Commun. **8**, 14956 (2017).

[23] Y. Zhou, D. Wu, Y. Zhu, Y. Cho, Q. He, X. Yang, K. Herrera, Z. Chu, Y. Han, and M. C. Downer, Out-of-plane piezoelectricity and ferroelectricity in layered – In_2Se_3 nanoflakes, Nano Lett. **17**, 5508 (2017).

[24] A. Chandrasekaran, A. Mishra, and A. K. Singh, Ferroelectricity, antiferroelectricity, and ultrathin 2D electron/hole gas in multifunctional monolayer MXene, Nano Lett. **17**, 3290 (2017).

[25] J. Xiao, H. Zhu, Y. Wang, W. Feng, Y. Hu, A. Dasgupta, Y. Han, Y. Wang, D. A. Muller, and L. W. Martin, Intrinsic two-dimensional ferroelectricity with dipole locking, Phys. Rev. Lett. **120**, 227601 (2018).

[26] F. Xue, X. He, J. R. A. Han, J. Zhang, Z. Liu, W. Hu, V. Tung, and J. He, Gate-tunable and multidirection-switchable memristive phenomena in a van der Waals ferroelectric, Adv. Mater. **31**, 1901300 (2019).

[27] M. Si, A. K. Saha, S. Gao, G. Qiu, J. Qin, Y. Duan, J. Jian, C. Niu, H. Wang, and W. Wu, A ferroelectric semiconductor field-effect transistor, Nat. Electron. **2**, 580 (2019).

[28] K. Yasuda, X. Wang, K. Watanabe, T. Taniguchi, and P. Jarillo-Herrero, Stacking-engineered ferroelectricity in bilayer boron nitride, Science **372**, 1458 (2021).

[29] C. Wang, L. You, D. Cobden, and J. Wang, Towards two-dimensional van der Waals ferroelectrics, Nat. Mater. **22**, 542552 (2023).

[30] S. Tongay, S. S. Varnoosfaderani, B. R. Appleton, J. Wu, and A. F. Hebard, Magnetic properties of MoS_2: Existence of ferromagnetism, Appl. Phys. Lett. **101**, 123105 (2012).

[31] H. Shi, H. Pan, Y. Zhang, and B. I. Yakobson, Strong ferromagnetism in hydrogenated monolayer MoS_2 tuned by strain, Phys. Rev. B **88**, 205305 (2013).

[32] N. Mounet, M. Gibertini, P. Schwaller, D. Campi, A. Merkys, A. Marrazzo, T. Sohier, I. Castelli, A. Cepellotti, G. Pizzi, and N. Marzari, Two-dimensional materials from high-throughput computational exfoliation of experimentally known compounds, Nat. Nanotechnol. **13**, 246 (2018).

[33] N. Miao, B. Xu, L. Zhu, J. Zhou, and Z. Sun, 2D intrinsic ferromagnets from van der Waals antiferromagnets, J. Am. Chem. Soc. **140**, 2417 (2018).

[34] B. Huang, G. Clark, E. Navarro-Moratalla, D. R. Klein, R. Cheng, K. L. Seyler, D. Zhong, E. Schmidgall, M. A. McGuire, and D. H. Cobden, Layer-dependent ferromagnetism in a van der Waals crystal down to the monolayer limit, Nature **546**, 270 (2017).

[35] C. Gong, L. Li, Z. Li, H. Ji, A. Stern, Y. Xia, T. Cao, W. Bao, C. Wang, and Y. Wang, Discovery of intrinsic ferromagnetism in two-dimensional van der Waals crystals, Nature **546**, 265 (2017).

[36] G. Kresse and J. Hafner, *Ab initio* molecular dynamics for liquid metals, Phys. Rev. B **47**, 558 (1993).

[37] P. E. Blöchl, Projector augmented-wave method, Phys. Rev. B **50**, 17953 (1994).

[38] J. P. Perdew, K. Burke, and M. Ernzerhof, Generalized gradient approximation made simple, Phys. Rev. Lett. **77**, 3865 (1996).

[39] P. E. Blöchl, O. Jepsen, and O. K. Andersen, Improved tetrahedron method for Brillouin-zone integrations, Phys. Rev. B **49**, 16223 (1994).

[40] S. Grimme, J. Antony, S. Ehrlich, and H. Krieg, A consistent and accurate *ab initio* parametrization of density functional dispersion correction (DFT-D) for the 94 elements H-Pu, J. Chem. Phys. **132**, 154104 (2010).

[41] L. Bengtsson, Dipole correction for surface supercell calculations, Phys. Rev. B **59**, 12301 (1999).

[42] M. Brandbyge, J.-L. Mozos, P. Ordejón, J. Taylor, and K. Stokbro, Density-functional method for nonequilibrium electron transport, Phys. Rev. B **65**, 165401 (2002).

[43] N. Papior, N. Lorente, T. Frederiksen, A. García, and M. Brandbyge, Improvements on non-equilibrium and

transport Green function techniques: The next-generation transiesta, Comput. Phys. Commun. **212**, 8 (2017).

[44] M. Büttiker, Y. Imry, R. Landauer, and S. Pinhas, Generalized many-channel conductance formula with application to small rings, Phys. Rev. B **31**, 6207 (1985).

[45] Y. Zhao, J. Zhang, S. Yuan, and Z. Chen, Nonvolatile electrical control and heterointerface-induced half-metallicity of 2D ferromagnets, Adv. Funct. Mater. **29**, 1901420 (2019).

[46] See the Supplemental Material at http://link.aps.org/supplemental/10.1103/PhysRevApplied.21.044033 for more simulation results on the structural, electronic, and quantum transport properties of $M\mathrm{Si_2P_4/Sc_2CO_2}$ (M = Mo, W) van der Waals heterostructures.

[47] Z. Fei, W. Zhao, T. A. Palomaki, B. Sun, M. K. Miller, Z. Zhao, J. Yan, X. Xu, and D. H. Cobden, Ferroelectric switching of a two-dimensional metal, Nature **560**, 336 (2018).

[48] L. Cao, X. Deng, G. Zhou, S. Liang, C. V. Nguyen, L. K. Ang, and Y. S. Ang, Multiferroic van der Waals heterostructure $\mathrm{FeCl_2/Sc_2CO_2}$: Nonvolatile electrically switchable electronic and spintronic properties, Phys. Rev. B **105**, 165302 (2022).

[49] G. Liu, T. Chen, G. Zhou, Z. Xu, and X. Xiao, Nonvolatile electrical control and reversible gas capture by ferroelectric polarization switching in 2D $\mathrm{FeI_2/In_2S_3}$ van der Waals heterostructures, ACS Sensors **8**, 1440 (2023).

[50] Y. Wu, J. Tong, L. Deng, F. Luo, F. Tian, G. Qin, and X. Zhang, Coexisting ferroelectric and ferrovalley polarizations in bilayer stacked magnetic semiconductors, Nano Lett. **23**, 6226 (2023).

[51] J. Kang, W. Liu, D. Sarkar, D. Jena, and K. Banerjee, Computational study of metal contacts to monolayer transition-metal dichalcogenide semiconductors, Phys. Rev. X **4**, 031005 (2014).

[52] R. T. Tung, Formation of an electric dipole at metal-semiconductor interfaces, Phys. Rev. B **64**, 205310 (2001).